Nanoscale

PAPER

View Article Online
View Journal | View Issue

Cite this: *Nanoscale*, 2026, **18**, 1619

High-temperature oxygen-assisted molecular beam epitaxy of $BaWO_4$ on W(110): growth mechanism and structural characterization

Clara Gutiérrez-Cuesta, *[a] Víctor Rojo,[a] José Emilio Prieto, [a] Anna Mandziak,[b] Pawel Nita,[b,c] Adolfo del Campo,[d] Natalia Kwiatek-Maroszek, [b] Iulia Cojocariu,[e,f] Marcin Szpytma, [e,g] Giovanni Fevola,[h] Arantzazu Mascaraque,[i] José F. Marco,[a] Tevfik Onur Menteş,[e] Andrea Locatelli,[e] Adrián Quesada [d] and Juan de la Figuera [a]

Received 15th September 2025,
Accepted 4th December 2025

DOI: 10.1039/d5nr03903g

rsc.li/nanoscale

We have studied the growth of barium tungstate, $BaWO_4$, by high-temperature oxygen-assisted molecular beam epitaxy on W(110). Barium tungstate grows in the form of isosceles triangular-shaped islands, tens of micrometers wide and tens of nanometers in height. The growth was monitored in real time by low-energy electron microscopy and characterized *in situ* by low-energy electron diffraction, X-ray absorption and X-ray photoelectron spectroscopies. Further *ex situ* characterization was performed by optical and atomic force microscopies and Raman spectroscopy. Barium tungstate growth on W(110) was performed by dosing only barium in a molecular oxygen atmosphere due to incorporation of W atoms from the W(110) substrate. The islands correspond to the $BaWO_4$ (011) crystallographic orientation and their sides are aligned along the [001] and [1$\bar{1}$1] directions of the $BaWO_4$ crystal.

1 Introduction

The controlled growth of complex oxides on metallic substrates is a critical area of research for developing functional materials with tailored electronic, optical and catalytic properties. Barium tungstate ($BaWO_4$) exhibits excellent optical transparency, high dielectric permittivity and luminescent properties,[1,2] making it a promising material for scintillators and other photonic[3–6] applications. Understanding the fundamental mechanisms governing the growth of $BaWO_4$ on W(110) and optimizing the deposition conditions is interesting for achieving high-quality films suitable for integration into functional devices.

$BaWO_4$ belongs to the scheelite family of tungstates,[7] represented by tungstates of large and electropositive divalent, alkaline-earth ions such as Ca^{2+}, Sr^{2+}, Ba^{2+} or Mg^{2+}. It comprises edge-sharing W^{6+} tetrahedral cations with the Ba^{2+} cation occupying octahedral interstitial sites in the structure, within a tetragonal unit cell. It belongs to the $I4_1/a$ space group. Their lattice parameters are $a = b = 5.65$ Å and $c = 12.7$ Å.[8] $BaWO_4$ has been previously grown by several methods, such as co-precipitation,[9,10] spray pyrolysis,[11] hydrothermal synthesis[12] or thermal gradient Czochralski crystal growth.[13] However, the epitaxial growth of $BaWO_4$ thin films on metallic substrates remains largely unexplored. W(110) appears to be an ideal substrate for such growth due to its well-defined crystallographic structure and strong affinity for oxygen, on which it forms a chemisorbed layer.[14,15]

Metallic substrates have long been used for the growth of ultrathin oxides,[16] as such oxides are amenable to the full range of surface science techniques. High-temperature oxygen-assisted molecular beam epitaxy produces highly crystalline thin films with well ordered surfaces, in particular of oxides. It enables the control of the deposited coverage in the range of atomic monolayers. The method allows *in situ* characterization of the structures using techniques such as PEEM or XPS directly after growth as it is performed in ultrahigh vacuum (UHV). However, it can be difficult to select which specific phase is grown. When growing tungstates by other procedures, such as hydrothermal methods, the phase, morphology and

[a]*Instituto de Química Física Blas Cabrera, CSIC, Madrid 28006, Spain. E-mail: cgutierrez@iqf.csic.es*
[b]*Solaris National Synchrotron Radiation Centre, Kraków 30-392, Poland*
[c]*Faculty of Physics, Astronomy and Applied Computer Science, Jagiellonian University, 30-348 Kraków, Poland*
[d]*Instituto de Cerámica y Vidrio, CSIC, Madrid E-28049, Spain*
[e]*Elettra-Sincrotrone Trieste S.C.p.A., S.S. 14 – km 163, 5 in AREA Science Park, 34149 Trieste, Italy*
[f]*Department of Physics, University of Trieste, Via A. Valerio 2, 34127 Trieste, Italy*
[g]*Faculty of Physics and Applied Computer Science, AGH University of Kraków, al. A. Mickiewicza 30, 30-059 Krakow, Poland*
[h]*Center for X-ray and Nano Science CXNS, Deutsches Elektronen-Synchrotron DESY, Notkestr. 85, 22607 Hamburg, Germany*
[i]*Universidad Complutense de Madrid and Unidad Asociada UCM-CSIC(IQF) "Surface Science and Magnetism of Low Dimensional Systems", Madrid 28040, Spain*

size can be controlled. On the other hand, it is not possible to observe the formation of the material in real time or to study the growth dynamics. The key point of our work is that this specific phase of barium tungstate can be obtained directly using high-temperature oxygen-assisted MBE, depositing only barium on a tungsten single crystal. It can be coupled to *in situ* observation of the growth by low-energy electron microscopy (LEEM)[17] allowing to explore a range of growth parameters in order to optimize the quality of the oxides. In such a way, we have grown equilateral triangular-shaped islands of spinels of magnetite,[18] cobalt ferrite,[19] and nickel ferrite[20] as well as rock-salt oxides such as cobalt oxide[21] and nickel oxide, mostly on 4d and 5d transition metal substrates. The quality of such oxide microcrystals is reflected in the observation of large ferri- or antiferromagnetic domains in remanence.[22–24] More recently, we have reported the growth of synthetic hübnerite nanowires on W(110) by the same procedure.[25]

In the present work, we investigate the growth by molecular beam epitaxy (MBE) of $BaWO_4$ on W(110) UHV conditions, focusing on the structural evolution, interface chemistry and film morphology. Using LEEM, we follow the growth of $BaWO_4$ in real time by depositing only Ba. The interaction between tungsten and oxygen during the initial nucleation stage is crucial to allow the tungsten to be incorporated in the $BaWO_4$ islands grown. These findings provide insights into the thermodynamic and kinetic factors governing the growth process and provide a novel path to grow $BaWO_4$ nanostructures with high crystalline quality.

2 Experimental

The experiments were performed using an Elmitec LEEM III instrument at the Blas Cabrera Institute of Madrid, the Elmitec SPELEEM III ones located at the DEMETER beamline of the Solaris synchrotron and at the Nanospectroscopy beamline of the Elettra synchrotron. Using LEEM mode, we observed the surface evolution in real time during the growth. We also imaged the surface using X-Ray Photoemission Electron Microscopy (XPEEM), with a soft X-ray beam for illumination at the synchrotron facilities.[26] In particular, selected area chemical information can be obtained using XPEEM and X-Ray Photoelectron Spectroscopy (XPS).

The substrate used for growth was a W(110) single crystal. It was cleaned by applying several flashes at 1500 °C in a molecular oxygen atmosphere of 1×10^{-6} mbar. Barium was evaporated either using baskets under direct heating by a filament, or by electron-beam bombardment. The Ba flux was calibrated by evaporating metallic barium on clean W(110) and monitoring the change in the work function to determine the time to obtain a third of a monolayer.[27] The typical deposition rate was one monolayer (ML) in 15 minutes.

Parameters such as temperature and oxygen partial pressure are crucial for obtaining highly-crystalline oxide nanostructures by MBE. We chose an oxygen partial pressure of 4×10^{-6} mbar as this is sufficient to oxidise the barium while enabling us to image the surface using LEEM. The temperature for growth was set as high as possible to promote better crystallinity. However, we observed that temperatures higher to 800 °C lead to the decomposition of the nanostructures. *In situ* structural and chemical characterization was performed using LEEM and low-energy electron-diffraction (LEED) as well as XPEEM. *Ex situ* analysis was performed by optical microscopy, atomic force microscopy (AFM) and Raman spectroscopy. The Raman spectra were acquired with a commercial Witec Alpha 300RA confocal Raman spectrometer, using a 100× objective with a numerical aperture of 0.95. The light source was a 532 nm laser operated at 1 mW power, selected in order to avoid modification of the samples. The average of the spectra presented is of 5 scans, each acquired with a 30 s integration time.

3 Results and discussion

In the following we describe in detail the results of depositing barium under a background of molecular oxygen at high temperature. After describing the morphology of the nanostructures obtained, we chemically characterize them with selected-area XPS, XAS, and finally Raman spectroscopy. Finally, having identified the phase of the barium oxide obtained, we determine the crystallographic orientation of the oxide.

3.1 Growth

LEEM can be used to monitor the growth in real time under the conditions employed in this work.[17] In Fig. 1 we present a schematic growth mechanism as well as selected frames from such a sequence acquired during the deposition of Ba. Fig. 1b shows the tungsten surface, at this stage covered by atomic oxygen after exposure to 4×10^{-6} mbar of molecular oxygen at 800 °C for several minutes. It contains terraces, atomic steps and other surface features characteristic of the crystal. While at elevated temperature no ordered superstructure LEED pattern is observed, from experiments performed with similar background pressures and cooling down to room temperature, it is known that the surface is covered with a nearly complete layer of chemisorbed oxygen.[15] The growth temperature was selected to be as high as possible to promote surface diffusion and thus good crystallinity. Upon starting to dose Ba, small dark structures are observed to appear at the substrate steps (Fig. 1c). Those structures grow upon continued deposition until they cover completely the surface after 15 min. Fig. 1c, was acquired just before that layer completion.

Deposition of aditional Ba results in the formation of new white regions, with a streaky aspect along two different directions (Fig. 1e). While these streaky structures remain unchanged, a new island, exhibiting different morphology, nucleates and grows rapidly, see right-hand side of Fig. 1f. This new island grows towards the bottom of the image in Fig. 1g, eventually covering a large surface area and branching into triangular regions. Dark lines, likely due to atomic steps, can be observed on its surface. The island shows a strong contrast with respect to the surrounding surface and develops into

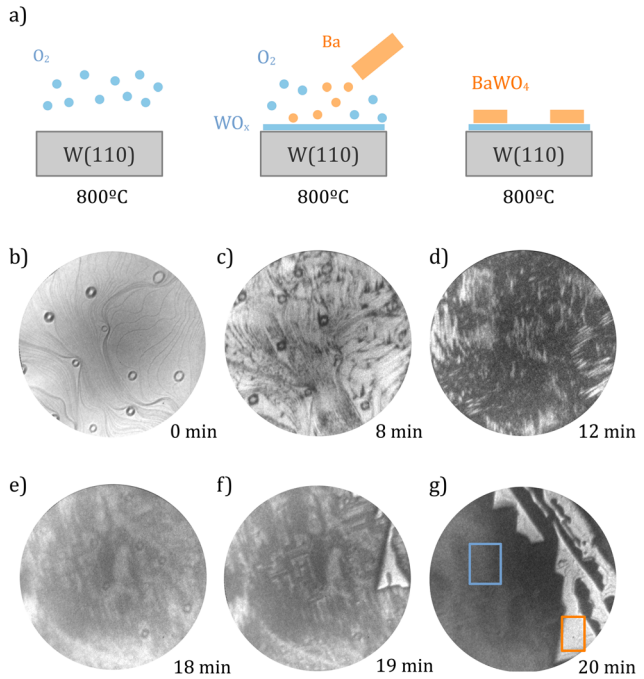

Fig. 1 (a) Schematic of the growth procedure. (b–g) Selected LEEM images from a sequence acquired during the deposition of Ba on the W(110) surface at 800 °C while exposing it to $P = 4 \times 10^{-6}$ mbar of O_2. The field of view is 10 μm. The deposition rate was 1 ML per 15 min and the total growth time t_{total} = 30 min. The wetting layer area is marked with a blue rectangle, and the island area with a orange rectangle.

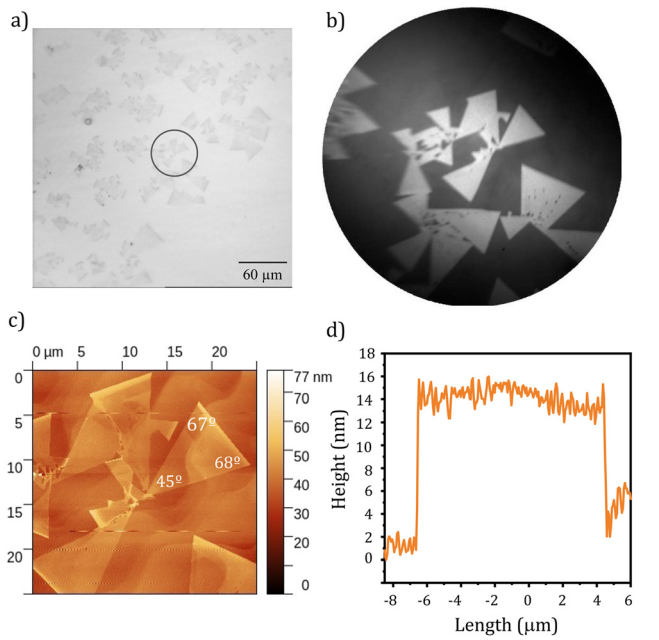

Fig. 2 Correlative microscopy of the islands. (a) Optical microscopy of a region of the sample, with a field of view of 0.5 mm. (b) XPEEM image on the area marked with a circle in (a) at the barium M_4 edge (784 eV), with a field of view of 75 μm. (c) AFM image of the same area, indicating the angles between the sides of one of the islands. (d) Height profile across one of the islands.

a ramified, connected structure spanning tens of microns. After reaching this stage, barium deposition was stopped and the sample was cooled down to room temperature in oxygen atmosphere. UHV conditions were restored before further characterization.

In summary, growth consists of the initial nucleation and growth of a layer that covers completely the surface (*i.e.* a wetting layer). After such layer is completed, well separated islands nucleate and grow. Therefore, the growth proceeds in an Stranski–Krastanov-like mode, as observed also for the growth of iron oxides on Ru(0001)[28] or Pt(111).[29] We note that unlike in metal growth, in oxide growth the two areas, wetting layer and islands, might correspond to different phases. Following the same convention, we likewise name the two regions observed in the final frame of Fig. 1f, the wetting layer (WL, blue rectangle), and the 3-dimensional islands (orange rectangle).

3.2 Topography

We have imaged the surface using various microscopy techniques to determine the geometry and height of the islands. In a different experiment, the islands were first grown under LEEM observation. Then the W(110) crystal was taken out of vacuum and observed by optical microscopy and AFM. After that, it was introduced in a PEEM system and the same area was located in PEEM images. Fig. 2a shows an optical microscopy image with a large field of view of 0.5 mm. The islands are clearly detectable. They appear darker than the wetting layer. They seem to be distributed in clusters and oriented along different directions, but they all exhibit the same fundamental shape, either of complete isosceles triangles or portions of such triangles.

A typical XPEEM image acquired at the photon energy of the Ba M_4 absorption edge maximum, 784 eV, is shown in Fig. 2b, which corresponds to the area marked with a circle in Fig. 2a. Careful observation of the image shows that each cluster of islands grows from a central point. The XPEEM image shows that the islands have more intensity than the wetting layer at that energy, which indicates that they contain more barium. The same area was explored using AFM in Fig. 2c, where the angles between the sides at one of the islands are indicated. The values of 67°, 68° and 45° confirm that the islands have an isosceles triangular shape. In Fig. 2d, a height profile from the AFM image shows that the island height is around 10 nm. Analyzing a large number of islands in the same way it was found that they are mostly regular in shape with flat top surfaces. Their morphology seems to be unaffected after removal from vacuum.

3.3 Chemical characterization

To gain information on the chemical composition of the different regions of the sample, *i.e.* the WL and the islands, we use selected-area XPS and XAS, both acquired in PEEM mode. The spatially resolved XPS spectra, measured *in situ*, was obtained in the region of the tungsten 4f core level in the two distinct regions of the sample (Fig. 3). The photon energy used

was 200 eV. The spectra were deconvoluted into its spin–orbit split $4f_{7/2}$ and $4f_{5/2}$ components. Each spin–orbit doublet was fitted using a Voigt function. A common Lorentzian full width at half maximum (FWHM) of 1.5 eV was imposed for all components. We have used a Shirley-type background, adequate for insulating or semiconducting oxide systems.

The resulting fits reveal distinct chemical environments associated with the tungsten species. In the wetting layer, Fig. 3a, there are three spin–orbit doublets. The main component appears at 31.4 eV and corresponds to metallic tungsten (blue). This component originates from the W(110) substrate. That this is the largest component implies that the wetting layer is few atomic layers thick, as a thicker film would attenuate the substrate signal when using electrons with kinetic energies close to the minimum of the mean free path universal curve.[30] The doublet with the $4f_{7/2}$ peak at 32 eV (orange) is related to oxygen chemisorbed on the tungsten.[31] Finally, at 35.6 eV (red), there is a component that corresponds to the W^{6+} oxidation state. This component suggests some intermixing between tungsten and the oxidized Ba in the wetting layer. This is in contrast with the case of oxides grown on Ru(0001), where no intermixing is detected.

Fig. 3b shows the spectrum obtained on the island. Here, the largest component is at 37 eV (pink), that corresponds to the W^{6+} oxidation state. There are four more contributions with much lower intensities. The one at 35.6 eV (red) is related to the W^{6+} oxidation state as well and the component at 34 eV (green) to W^{4+}, suggesting that there is a gradient of oxidation states of tungsten in the islands. Finally, we also observe contributions at 32.2 eV (orange) and 31.4 eV (blue) that correspond, respectively to oxygen adsorbed on the tungsten and metallic tungsten. We note that the islands may be insulating, and some of the observed low intensity signals might exhibit some charging.

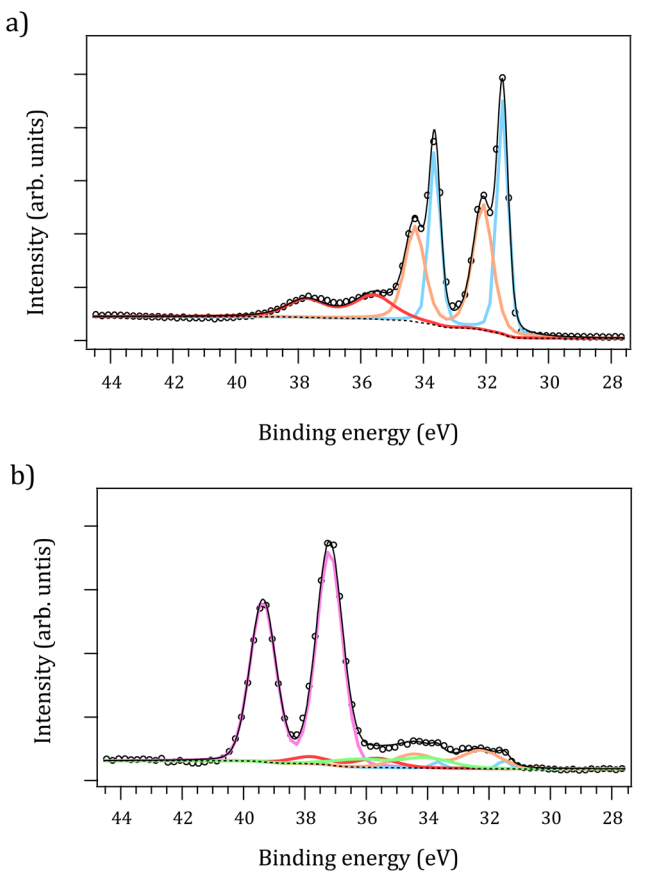

Fig. 3 Selected-area XPS spectra acquired (a) On the wetting layer and (b) on top of a 3D island. The photon energy is 200 eV.

Thus, XPS helps us to conclude that the wetting layer is quite thin and that the islands are mostly composed of tungsten in the W^{6+} oxidation state. Given the height of the islands, which is of the order of ten nanometers (see Fig. 2d), the observed oxidized tungsten cannot be located at the island interface with the wetting layer but must correspond to the main component of the islands. As tungsten was not deposited on the surface, it must come from the W(110) crystal.

The fact that oxidized tungsten is found in the 3D islands formed upon barium deposition in oxygen is likely related to the formation of volatile tungsten oxides upon oxygen exposure. Indeed, it is a well known fact that tungsten can be readily etched by exposing it to oxygen at high temperatures. This observation is at the origin of modern surface science as reported by the seminal works of Irving Langmuir.[32] In the late last century it was studied how exposing tungsten at high temperatures to oxygen pressures even in the 10^{-6} mbar range can induce the evaporation of oxides of several types.[33,34] Although our temperature is below the ones employed in those studies, it is likely that WO_x units are formed on the W(110) surface and diffuse distances up to tens of micrometers, providing a source of W^{6+} to be incorporated into the growing islands. Thus the islands are composed most probably of a mixed barium-tungsten oxide. We note that high diffusivity of adatoms in the presence of adsorbed oxygen or hydrogen has long been observed, as the bond with the adsorbate can weaken the bond with the substrate, and thus lower the diffusion barrier. This has been named the "sky-hook" effect.[35–38] Future work is planned to further characterize those possible tungsten carriers.

XAS-PEEM offers an effective means of determining the oxidation state of barium. XAS spectra of the Ba $M_{4,5}$ edges are displayed in Fig. 4a, for the islands (orange) and the wetting layer (blue). The energies of the main peaks are 784 eV and 799 eV. These correspond to Ba^{2+}.[39] The Ba absorption signal is considerably stronger in the islands, even though there is some signal also from the wetting layer.

The O K-edge spectrum is presented in Fig. 4b. The spectrum from the wetting layer, which shows a very weak oxygen signal, is dominated by oxygen absorption on the X-ray optics prior to the PEEM instrument. It has been used for normalization of the island spectra. In oxides, the oxygen K-edge XAS spectrum corresponds to the transition from the 1s core level to the unoccupied 2p band,[40] and it reflects the unoccupied density of states of the oxygen anion.[41] In our case, the two most intense peaks appear at energies of 531.6 eV and 533.2 eV respectively, with a difference of 1.6 eV. At higher energies some smaller peaks can be observed near 537 eV and 543 eV.

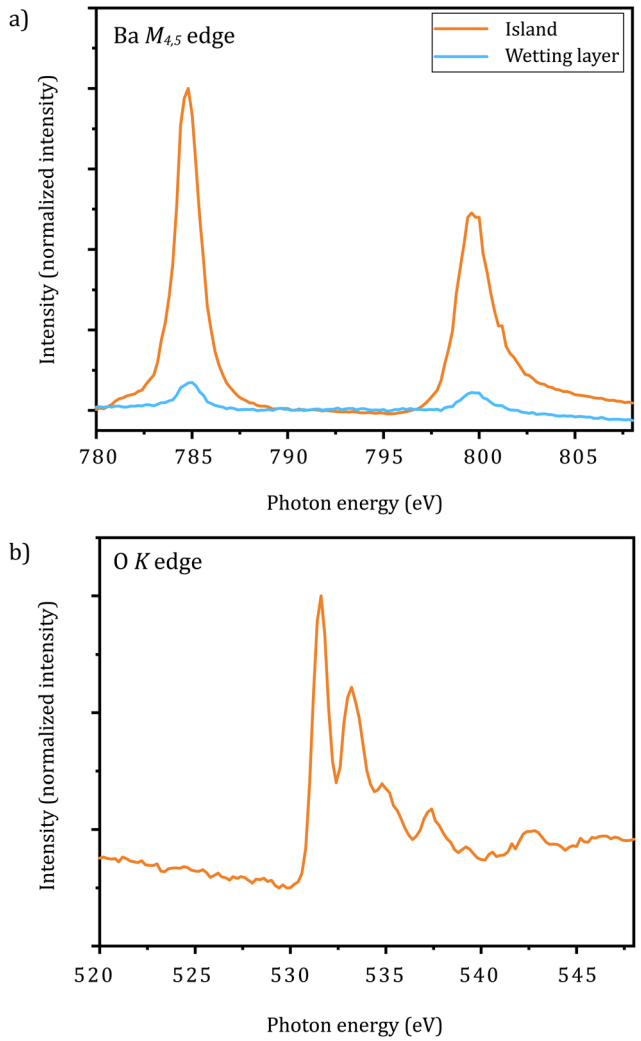

Fig. 4 (a) XAS spectra at the Ba $M_{5,4}$ edges on the island (orange) and wetting layer (blue) and (b) XAS spectra of the O K-edge of the island.

Given the presence of oxygen and W^{6+} in the islands, the most likely explanation for the two most intense peaks is that they arise from hybridization of the oxygen 2p with the 5d states from W^{6+}, which, when tungsten is surrounded by oxygen according to the ligand field theory,[42] split into the t_{2g} and e_g bands. The separation of the bands, which gives directly the crystal field parameter$10D_q$, and their sequence on the energy scale depend on the particular oxygen configuration around W^{6+}. We have reported that for $MnWO_4$ nanowires, which have the wolframite structure with octahedral W^{6+} units,[25] the energy difference between the peaks and thus $10D_q$ is 4 eV. In our case, it amounts to 1.6 eV. This difference can be explained if the coordination for the observed W^{6+} is tetrahedral instead of octahedral,[43] in agreement with the factor of 4/9 of the crystal-field splitting between the t_{2g} and e_g levels in both environments. In such case, the first peak at 531.6 eV should correspond to the hybridization of the oxygen 2p band with the tungsten e_g ones, which are lower in energy for a tetrahedral arrangement, while the 533.2 eV peak corresponds to hybridization with the tungsten t_{2g} bands. This interpretation of the oxygen spectra implies that tungsten in the islands is located in a tetrahedral environment.

3.4 Raman vibrational modes

Raman spectroscopy is a technique which has long been used to determine the presence of particular tungstate groups.[44] In the present case, we have already determined that our islands are composed of Ba^{2+} and W^{6+}, the latter in a tetrahedral environment. From the possible mixed oxides, $BaWO_4$ with the scheelite structure is the most stable one. This structure is composed of tungsten atoms in a tetrahedral environment and Ba atoms in an octahedral environment, sharing edges between them. We measured the Raman spectrum from a single $BaWO_4$ island using spot-Raman, as shown in Fig. 5. The spectrum is dominated by the highest intensity mode at 925 cm^{-1}. The tetragonal scheelite structure has 13 modes expected to be Raman-active: $3A_g + 5B_g + 5E_g$. Two of these modes are reported to overlap, but all of them have been observed in high-quality bulk crystals. As shown in Table 1, the spectrum of the scheelite $BaWO_4$ structure has been reported in ref. 45. 11 modes are detected at the islands, which differ at most by 4 cm^{-1} from the literature values, and often by less than 1 cm^{-1}. This clearly indicates that our nanoislands are of very high crystalline quality. It is also relevant that the crystals are thick enough to avoid observation of any strain effects caused by the substrate (which are expected to shift the Raman peaks to some extent) or any confinement effects. No Raman signal is observed outside the islands on the wetting layer. According to the XPS analysis, the layer is primarily composed of adsorbed tungsten and oxygen, with minor components of W^{4+} and W^{6+}. We suggest that it is not a continuous monolayer, but rather small clusters of WO_x that cover the substrate unevenly.

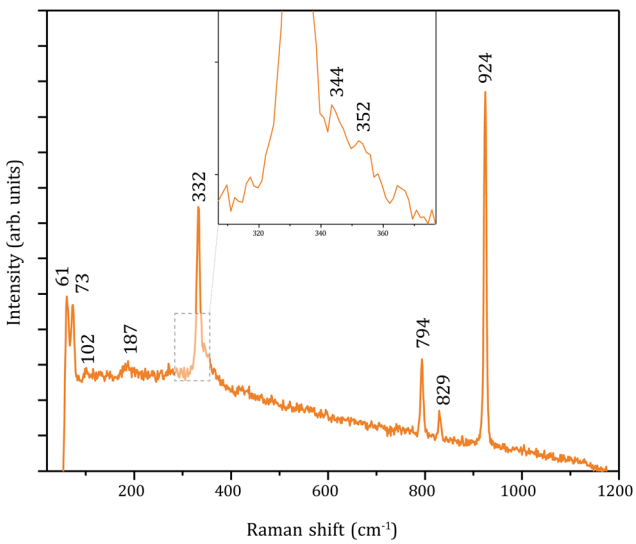

Fig. 5 Raman spectra acquired on the $BaWO_4$ islands. 11 of the 13 predicted vibrational modes are detected (see Table 1).

Table 1 Raman modes detected in the nanoislands, compared with those found in the reference work in ref. 45

Mode	Ref. 45 (cm^{-1})	This work (cm^{-1})
A_g	925	924
B_g	831	829
E_g	795	794
E_g	353	352
B_g	345	344
B_g	332	332
A_g	332	332
E_g	191	187
A_g	150	—
B_g	132	—
E_g	101	102
E_g	75	73
B_g	63	61

3.5 Orientation

Having confirmed that the islands are composed of $BaWO_4$, it remains to determine which crystal face is exposed and the reason why they present shapes of isosceles triangles. To study the crystalline structure, we employed microspot LEED using a LEEM instrument. LEED patterns were acquired at several energies. An example recorded at 26 eV on an island is shown in Fig. 6a. It is remarkable that the pattern survives exposure to air. The pattern shows well-defined diffraction spots arranged in an oblique lattice. The reciprocal lattice unit cell is defined by the two vectors marked in the image. The $BaWO_4$ a_2^* vector is closely aligned with the first-order $[\bar{1}12]$ diffraction spot, with a small deviation by an angle of 8°. Using as a reference the LEED pattern of W(110) before growing the barium oxide, we can calibrate the scale of the $BaWO_4$ unit cell. The two reciprocal space vectors have lengths of $a_1^* = 1.20\,\text{Å}^{-1}$ and $a_2^* = 0.90\,\text{Å}^{-1}$, forming an angle of 113°.

In real space, those vectors translate into an oblique unit cell with vectors which are separated by 67°, and are a_1 = 5.65 Å and a_2 = 7.82 Å long respectively. The a_1 vector length is in good agreement with the [100] basis vector of the $BaWO_4$ unit cell, while a_2 fits closely one half of the [111] one, with a residual mismatch of 4%. Furthermore, these directions make an angle of 67.8° in $BaWO_4$. This indicates that the surface of the islands is oriented along the (011) face of the body-centered tetragonal $I4_1/a$ scheelite structure. A model of the scheelite crystalline structure is displayed in Fig. 6b, with the (011) plane marked (blue corresponds to oxygen, orange to barium and grey to W). An atomic model obtained by cutting the bulk structure along a (011) plane is shown in Fig. 6c (in the cut shown, the tungsten atoms are covered by the barium and oxygen ones). The two directions are shown in the figure, and it can be seen that the angles are in good agreement with the observed angles of the $BaWO_4$ islands, as it is shown in Fig. 2c. Thus, the sides of the islands are aligned along the [100] and $[1\bar{1}1]$ directions, and the exposed surface corresponds to a [1 × 1] bulk $BaWO_4$ (011) structure.

The optical microscopy image in Fig. 2a shows that the triangles have different orientations. To determine their relationship with the compact directions of the substrate, we studied the relative orientation of 126 triangles. Fig. 6d shows the four scenarios encountered. First, the short side of the triangle can be oriented along the $[\bar{1}12]$ direction of the W(110) crystal with an angle mismatch of 8°, which is consistent with the angle deviation observed in the LEED pattern. This is shown in the first panel of Fig. 6d. It can also be oriented along the $[\bar{1}10]$ direction (second panel of Fig. 6d). We observed that one of the long sides of the triangles can be oriented along the $[\bar{1}12]$ and the $[1\bar{1}2]$ or the $[\bar{1}10]$ directions, with the same angle deviation, as shown in the bottom panels of Fig. 6d. In this case we only found two of the four orientations expected in the area under observation, being the ones with the long axis of the triangle oriented along the $[1\bar{1}2]$ and the $[1\bar{1}\bar{2}]$ directions.

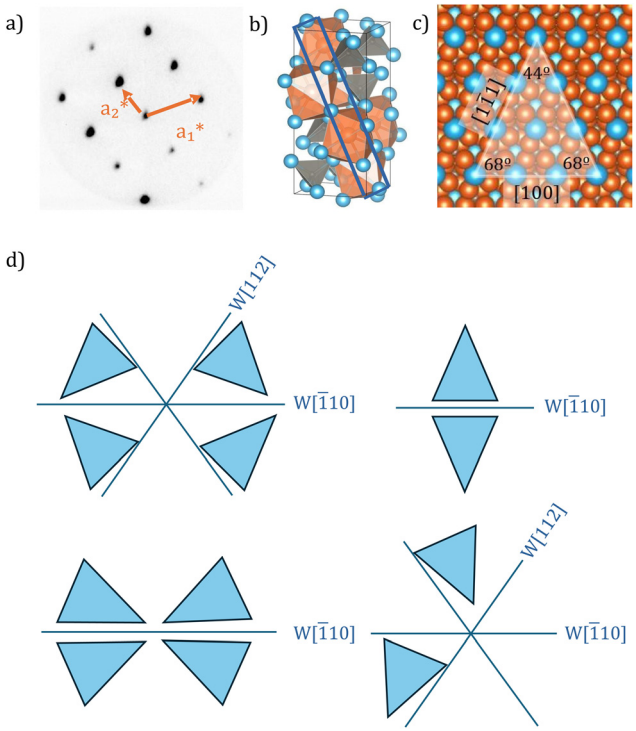

Fig. 6 (a) LEED pattern from a $BaWO_4$ island, at a start voltage of 26 V. The lattice vectors are marked with arrows, (b) schematic of the scheelite $BaWO_4$ unit cell, drawn using VESTA[46] (oxygen in blue, barium in orange and tungsten in gray). The W tetrahedra and the Ba octahedra are also shown. (c) Cut along a (011) plane of the $BaWO_4$ structure which shows a Ba termination displayed showing the preferential growth directions of the islands. No attempt has been made to model a realistic surface, so only the directions and angles should be relied upon. (d) Different orientations of the triangles relative to the compact directions of the W(110) substrate.

4 Conclusions

We have deposited barium on W(110) substrate by high-temperature oxygen-assisted molecular beam epitaxy. This gives rise to an ultrathin wetting layer that completely covers the substrate and to clusters of islands tens of microns wide and

around 10 nm thick. The islands have the shape of isosceles triangles with one angle of 44° and two of 68°. The islands are composed of Ba^{2+} and W^{6+}, the latter in a tetrahedral environment, as determined from selected area XPS and XAS measurements. The wetting layer consists mostly of Ba^{2+} and chemisorbed oxygen. Raman spectra unequivocally confirm that the structure of the islands corresponds to the scheelite phase of $BaWO_4$. The islands show a clear LEED pattern which corresponds to a (1 × 1) $BaWO_4$ (011) orientation with the sides of the islands nearly parallel to the [100] and [1$\bar{1}$1] high symmetry directions of the scheelite structure. The tungsten substrate provides the required W^{6+} cations likely from highly mobile WO_x units generated by the exposure of the W(110) crystal to molecular oxygen at high temperatures. We propose that this supply of tungsten provides a simple method to obtain $BaWO_4$ islands with high crystalline quality that can be used as a starting point for further research on this material. The very well-defined triangular shape together with their nanoscale dimensions of the $BaWO_4$ islands, combined with their optical properties, opens the way to the use of these nanostructures in photonic applications such as nanolasers or nanowaveguides.

Author contributions

C. Gutiérrez-Cuesta: investigation, writing – original draft. V. Rojo: investigation. J. E. Prieto: investigation, project administration, writing – review & editing. A. Mandziak: investigation, writing – review & editing. P. Nita: investigation, writing – review & editing. A. del Campo: investigation. N. Kwiatek-Maroszek: investigation, writing – review & editing. I. Cojocariu: investigation, writing – review & editing. M. Szpytma: investigation, writing – review & editing. G. Fevola: investigation, writing – review & editing. A. Mascaraque: investigation, writing – review & editing. J. F. Marco: investigation, writing – review & editing. T. O. Mentes: investigation, writing – review & editing. A. Locatelli: investigation, writing – review & editing. A. Quesada: investigation, writing – review & editing. J. de la Figuera: conceptualization, investigation, project administration, writing – original draft.

Conflicts of interest

There are no conflicts to declare.

Data availability

Data are available at the DIGITAL.CSIC open repository under http://hdl.handle.net/10261/409583.

Acknowledgements

This work was supported by Grants PID2021-124585NB-C31 and PID2021-124585NB-C33, funded by MCIN/AEI/10.13039/501100011033 and by "ERDF A way of making Europe"; by grant Mag4TIC-CM funded by the TEC-2024/TEC-380 program of the Comunidad de Madrid and by the BEETHOVEN project funded by the European Commission under grant agreement 101129912. It was also funded by the European Union as part of the Horizon Europe call HORIZON-INFRA-2021-SERV-01 under grant agreement number 101058414 and co-funded by UK Research and Innovation (UKRI) under the UK government's Horizon Europe funding guarantee (grant number 10039728) and by the Swiss State Secretariat for Education, Research and Innovation (SERI) under contract number 22.00187. Views and opinions expressed are however those of the author(s) only and do not necessarily reflect those of the European Union or the European Education and Culture Executive Agency (EACEA) or the UK Science and Technology Facilities Council or the Swiss State Secretariat for Education, Research and Innovation (SERI). Neither the European Union nor EACEA or the granting authorities can be held responsible for them. This work has received support from the European Union under the Horizon Europe programme, project NEPHEWS – Neutrons and Photons Elevating Worldwide Science (No. 101131414).

References

1 L. S. Cavalcante, J. C. Sczancoski, L. F. Lima, J. W. M. Espinosa, P. S. Pizani, J. A. Varela and E. Longo, *Cryst. Growth Des.*, 2009, **9**, 1002–1012.
2 Y. Wang, H. Gao, S. Wang, L. Fang, X. Chen, C. Yu, S. Tang, H. Liu, Z. Yi and H. Yang, *Adv. Powder Technol.*, 2021, **32**, 4186–4197.
3 Z. Barzgari, S. Z. Askari and A. Ghazizadeh, *Mater. Sci. Semicond. Process.*, 2015, **33**, 36–41.
4 G. Yanalak, A. Ozen, A. Sarılmaz, A. Keles, E. Aslan, F. Ozel and I. Hatay Patir, *J. Phys. Chem. Solids*, 2022, **168**, 110821.
5 Y. Shi, J. Shi and C. Dong, *Opt. Mater.*, 2018, **84**, 396–403.
6 M. Hemmati, *Ceram. Int.*, 2022, **48**(18), 26508–26518.
7 E. Lassner and W.-D. Schubert, in *Tungsten: properties, chemistry, technology of the element, alloys, and chemical compounds*, Springer US, Boston, MA, 1999.
8 M. Patnaik, P. Yadav, E. Rout, A. Yadav, S. Jha, M. Tyagi and Sonu, *Radiat. Phys. Chem.*, 2024, **223**, 111957.
9 M. C. Oliveira, L. Gracia, I. C. Nogueira, M. F. do Carmo Gurgel, J. M. R. Mercury, E. Longo and J. Andrés, *Ceram. Int.*, 2016, **42**, 10913–10921.
10 C. Sridhar, Neha, Y.-S. Seo, I. Rabani, G. Turpu, S. Tigga and G. Padmaja, *Curr. Appl. Phys.*, 2024, **58**, 79–90.
11 A. R. Patil, L. D. Namade, T. D. Dongale and K. Y. Rajpure, *Colloids Surf., A*, 2025, **723**, 137352.
12 L. Alencar, A. Mesquita, C. A. Feitosa, R. Balzer, L. F. Probst, D. C. Batalha, M. G. Rosmaninho, H. V. Fajardo and M. I. Bernardi, *Ceram. Int.*, 2017, **43**, 4462–4469.
13 V. Caracciolo, F. Cappella, R. Cerulli, A. D. Marco, M. Laubenstein, S. Nagorny, O. Safonova and V. Shlegel,

Nucl. Instrum. Methods Phys. Res., Sect. A, 2018, **901**, 150–155.
14 K. Radican, S. I. Bozhko, S.-R. Vadapoo, S. Ulucan, H.-C. Wu, A. McCoy and I. V. Shvets, *Surf. Sci.*, 2010, **604**, 1548–1551.
15 D. Wilgocka-ŚlÈ©zak, T. Giela, K. Freindl, N. Spiridis and J. Korecki, *Appl. Surf. Sci.*, 2020, **528**, 146712.
16 H.-J. Freund, *J. Am. Chem. Soc.*, 2016, **138**, 8985–8996.
17 J. I. Flege and D. C. Grinter, *Prog. Surf. Sci.*, 2018, **93**, 21–45.
18 M. Monti, B. Santos, A. Mascaraque, O. Rodríguez de la Fuente, M. A. Niño, T. O. Menteş, A. Locatelli, K. F. McCarty, J. F. Marco and J. de la Figuera, *Phys. Rev. B: Condens. Matter Mater. Phys.*, 2012, **85**, 020404.
19 L. Martín-García, A. Quesada, C. Munuera, J. F. Fernández, M. García-Hernández, M. Foerster, L. Aballe and J. de la Figuera, *Adv. Mater.*, 2015, **27**, 5955–5960.
20 A. Mandziak, J. d. l. Figuera, S. Ruiz-Gómez, G. D. Soria, L. Pérez, P. Prieto, A. Quesada, M. Foerster and L. Aballe, *Sci. Rep.*, 2018, **8**, 17980.
21 A. Mandziak, G. D. Sori, J. E. Prieto, P. Prieto, C. Granados-Miralles, A. Quesada, M. Foerster, L. Aballe and J. de la Figuera, *Sci. Rep.*, 2019, **9**, 13584.
22 S. Ruiz-Gomez, L. Perez, A. Mascaraque, A. Quesada, P. Prieto, I. Palacio, L. Martin-Garcia, M. Foerster, L. Aballe and J. de la Figuera, *Nanoscale*, 2018, **10**, 5566–5573.
23 S. Ruiz-Gómez, A. Mandziak, L. Martín-García, J. E. Prieto, P. Prieto, C. Munuera, M. Foerster, A. Quesada, L. Aballe and J. de la Figuera, *Appl. Surf. Sci.*, 2022, **600**, 154045.
24 A. Mandziak, J. de la Figuera, A. Quesada, A. Berja, C. Granados-Miralles, J. E. Prieto, L. Aballe, M. Foerster, M. A. Nino and P. Nita, *Ultramicroscopy*, 2023, **253**, 113795.
25 K. Fornal, C. Gutierrez-Cuesta, A. del Campo, A. Mandziak, P. Nita, J. E. Prieto, J. F. Marco and J. de la Figuera, *J. Mater. Chem. C*, 2025, **13**(40), 20602–20608.
26 A. Locatelli, L. Aballe, T. O. Mentes, M. Kiskinova and E. Bauer, *Surf. Interface Anal.*, 2006, **38**, 1554–1557.
27 D. A. Gorodetsky and Y. P. Melnik, *Surf. Sci.*, 1977, **62**, 647–661.
28 B. Santos, E. Loginova, A. Mascaraque, A. Schmid, K. McCarty and J. de la Figuera, *J. Phys.:Condens. Matter*, 2009, **21**, 314011.
29 W. Weiss and W. Ranke, *Prog. Surf. Sci.*, 2002, **70**, 1–151.
30 C. J. Powell and A. Jablonski, *Surf. Interface Anal.*, 2002, **33**, 211–229.
31 R. X. Ynzunza, R. Denecke, F. J. Palomares, J. Morais, E. D. Tober, Z. Wang, F. J. G. Garcia de Abajo, J. Liesegang, Z. Hussain, M. A. Van Hove and C. S. Fadley, *Surf. Sci.*, 2000, **459**, 69–92.
32 I. Langmuir, *J. Am. Chem. Soc.*, 1913, **35**, 105–127.
33 J. C. Batty and R. E. Stickney, *J. Chem. Phys.*, 1969, **51**, 4475–4484.
34 A. E. Lee, K. E. Singer and D. Tabor, *Proc. R. Soc. London, Ser. A*, 1971, **323**, 523–539.
35 M. Kalff, G. Comsa and T. Michely, *Phys. Rev. Lett.*, 1998, **81**, 1255–1258.
36 S. Horch, H. Q. Lorensen, S. Helveg, E. Lægsgaard, I. Stensgaard, K. W. Jacobsen, J. K. Nørskov and F. Besenbacher, *Nature*, 1999, **398**, 134.
37 P. J. Feibelman, *Phys. Rev. Lett.*, 2000, **85**, 606–609.
38 W. Ling, N. Bartelt, K. Pohl, J. de la Figuera, R. Hwang and K. McCarty, *Phys. Rev. Lett.*, 2004, **93**, 166101.
39 D. Wlodarczyk, M. Amilusik, K. M. Kosyl, M. Chrunik, K. Lawniczak-Jablonska, M. Strankowski, M. Zajac, V. Tsiumra, A. Grochot, A. Reszka, A. Suchocki, T. Giela, P. Iwanowski, M. Bockowski and H. Przybylinska, *ACS Omega*, 2022, **7**, 18382–18408.
40 F. Frati, M. O. J. Y. Hunault and F. M. F. de Groot, *Chem. Rev.*, 2020, **120**, 4056–4110.
41 F. M. F. de Groot, M. Grioni, J. C. Fuggle, J. Ghijsen, G. A. Sawatzky and H. Petersen, *Phys. Rev. B: Condens. Matter Mater. Phys.*, 1989, **40**, 5715–5723.
42 C. BallHausen, *Introduction to Ligand Field Theory*, McGraw-Hill, New York, 1962.
43 S. G. Minasian, J. M. Keith, E. R. Batista, K. S. Boland, J. A. Bradley, S. R. Daly, S. A. Kozimor, W. W. Lukens, R. L. Martin, D. Nordlund, G. T. Seidler, D. K. Shuh, D. Sokaras, T. Tyliszczak, G. L. Wagner, T.-C. Weng and P. Yang, *J. Am. Chem. Soc.*, 2013, **135**, 1864–1871.
44 T. Basiev, A. Sobol, P. Zverev, L. Ivleva, V. Osiko and R. Powell, *Opt. Mater.*, 1999, **11**, 307–314.
45 I. Carvalho, R. Sousa, J. Matos, J. Moura, P. Freire, G. Pinheiro and C. Luz-Lima, *J. Mol. Struct.*, 2020, **1204**, 127498.
46 K. Momma and F. Izumi, *J. Appl. Crystallogr.*, 2011, **44**, 1272–1276.